1	
2	In Situ Polymerization of Polypyrrole and Polyaniline on the Surface of
3	Magnetic Molybdenum Trioxide Nanoparticles: Implications for Water
4	Treatment
5	Sofia K. Fanourakis ¹ , Sharona Q. Barroga ^{2,3} , Jem Valerie D. Perez ² , Lilin He, ⁴ Debora F.
6	$Rodrigues^{I,5*}$
7	
8	
9	¹ Department of Materials Science and Engineering, University of Houston, Houston, TX 77204
10	-4003
11	² Department of Chemical Engineering, University of the Philippines,
12	³ Department of Chemical Engineering, Mariano Marcos State University,
13	⁴ Neutron Scattering Division, Oak Ridge National Laboratory, Oak Ridge, Tennessee 37831-
14	6393, United States
15	⁵ Department of Civil and Environmental Engineering, University of Houston, Houston, TX
16	77204 - 4003
17	
18	* Corresponding Author: Debora F. Rodrigues, email: dfrigirodrigues@uh.edu
19	* Co-corresponding Author: Lilin He, email: <u>he3@ornl.gov</u>
20	

Abstract

Photocatalyst dissolution greatly diminishes the usability of photocatalysts in water treatments. Coating conductive polymers on the surface of photocatalysts can reduce dissolution without compromising the photocatalytic properties of the material. In this investigation, polypyrrole (PPy) and polyaniline (PANI) were used to coat two magnetic MoO₃ nanoparticles with different surface chemistries. The polymer-coated MoO₃@Fe₃O₄ nanoparticles were synthesized by optimizing the mole fractions of PPy or PANI, MoO₃, and Fe₃O₄. The optimized PPy@ MoO₃@Fe₃O₄ (PMF₁) and PANI@ MoO₃@Fe₃O₄ (PMF₂) resulted in 95.39 and 75.98% methylene blue dye removal, respectively. MoO₃ dissolutions of 4.12 and 5.6% were obtained for PMF₁ and PMF₂, respectively, demonstrating the reduced solubility of the coated nanoparticles as compared to their uncoated counterparts (7.87% for MF₁ and 18.1% for MF₂). In situ small-angle neutron scattering (SANS) was utilized to investigate the polymerization kinetics of PPy and PANI on nanoparticles. The results revealed that an increase in base material oxygen vacancies resulted in the reduction of both the polymer size and the polymerization rate. This study demonstrated that SANS provides valuable insights into the polymer growth mechanisms on nanoparticle surfaces.

Keywords: polymerization, pyrrole, aniline, photocatalyst, neutron scattering, magnetite, MoO₃.

1. Introduction

40

41

42

43

44

45

46

47

48

49

50

51

52

53

54

55

56

57

58

59

60

61

62

In recent years, molybdenum oxides including MoO₂, MoO₃, and other forms of MoO_{3-x} (2 < x < 3) have attracted enormous research efforts due to their broad applicability in catalysis, sensing, energy storage, biomaterials, and field emission devices. (1,2) Among these, MoO₃ has a wide bandgap (2.8–3.2 eV) with 20–30% ionic character for high visible light photocatalytic activity, thus favoring its use in photocatalysis for water treatment. (3,4) Furthermore, introducing a magnetic core, i.e., Fe₃O₄, into MoO₃ can ease the removal of the nanoparticles via the use of magnetic separation instead of filtration techniques, which makes the nanocomposite particularly appealing for use in water treatment.(5) However, MoO₃ nanomaterials and modified MoO₃ nanocomposites are partially soluble in water, especially in neutral and basic conditions, (4) which has hindered their use in the photocatalytic degradation of different organic pollutants such as dyes,(6) phenols,(7) volatile organic compounds (VOCs),(8) antibiotics,(9) and heavy metals.(10) The dissolution rate of MoO₃ in aqueous systems is impacted by the size, crystallinity, shape, surface area, and exposed plane of the nanomaterial.(3) To overcome this problem, MoO₃ nanostructures require modifications to improve their stability and decrease their dissolution to be utilized under neutral and basic conditions.

A suitable solution to solve the dissolution and reusability issues of nanoparticles is to coat them with polymers. For instance, polypyrrole (PPy) was used to coat cerium dioxide (CeO₂) nanoparticles for the reduction of Cr⁶⁺. The polymer-coated nanoparticle exhibited higher stability and reusability compared to pure CeO₂ due to the shell of PPy that prevents dissolution of the CeO₂ core.(11) PPy on the surface of MoO₃ was also prepared as an anode material on aqueous supercapacitors and demonstrated that the dissolution of molybdenum during the cycling process was prevented due to the presence of a PPy coating layer.(12) Furthermore, when PPy layers were

fabricated on MoO₃ microrods, the underlying MoO₃ 1D structure was preserved in the material's conversion to PPy@MoS₂, when without the coating the microrod structure completely collapsed, indicating the necessity of the polymer layer in the stabilization of the material.(13) In addition to dissolution and stability, polymer coatings can also add benefits to the properties of the nanoparticles. For instance, conductive polymers, such as PPy and PANI, have been used as coatings on nanomaterials due to their electrochemical, magnetic, and optical properties, low cost, and good environmental stability.(13,14) These properties make them good candidates for coating MoO₃-based materials. As PPy and PANI coatings have shown to improve the reusability and stability of metal oxide nanoparticles, we expect that the coatings will have a similar effect on our nanoparticles, which, uncoated, tend to dissolve in neutral pH conditions. Furthermore, the π -conjugated electron-rich systems of conductive polymers help inject electrons into the conduction band of semiconductor oxides, making them good candidates for utilization in visible light photocatalysis.(15)

In this study, we selected PPy and PANI to coat magnetic MoO₃ nanoparticles because these polymers can improve material stability, have a high electron–hole carrying capacity, and have been shown to enhance light absorption capacity as well as enhance charge separation of photoexcited charge carriers, which we expect to enhance the performance of the MoO₃ nanoparticles.(11,16) When they are mixed with transition metal oxide nanoparticles, the resulting material exhibits good photocatalytic performance.(11,16) For instance, coating of PPy or PANI on semiconductor photocatalysts, such as MoO₃/PPy,(17) PPy/TiO₂,(18) PANI/ZnO, PANI/CoFe₂O₄, PANI/CeO,(16) and PPy-BiOI,(19) resulted in a higher efficiency of organic dye degradation. Additionally, PPy-encapsulated V₂O₅ nanohybrids showed enhanced degradation of ciprofloxacin and erythromycin antibiotics when exposed to visible light, which was attributed to

the enhanced charge transfer properties due to the presence of PPy.(15) PPy coatings also exhibited high photocatalytic activity in the reduction of hazardous Cr⁶⁺ to Cr³⁺ due to the increased electron transfer rate in the synthesized CeO₂@PPy.(15) Furthermore, CeO₂@PPy exhibited higher reusability and stability compared to pure CeO₂.(11) Overall, various studies on the applications of PPy and PANI on semiconductor photocatalysts have reported improved photocatalytic activity of the nanomaterials they were coating.

While previous studies have shown the improvement of the nanomaterial properties via coatings with conductive polymers, there is a lack of studies investigating the parameters controlling the polymerization and their influences on the properties of the final polymernanoparticle composite. Many techniques have already been employed to indirectly investigate chain growth kinetics on different bulk materials including monitoring the change of monomer concentrations, (20) monitoring changes in pH or temperature, which might yield nonconducting oligomers, (21) and utilizing neutron scattering, X-ray scattering, and light scattering techniques coupled with computational modeling to directly monitor the chain size with reaction time. (22,23) Experimental data in conjunction with chemical calculations and computer simulations have allowed for the development of a number of theories regarding the polymerization kinetics of different polymers. (24) However, to our knowledge, little research has been conducted on the growth kinetics of the polymer chains on the surface of nanoparticles during polymerization. Obtaining such information is challenging but allows us to elucidate how nanoparticle surface chemistry can affect the polymerization process and in turn better control the properties of coated nanocomposites.

In the present work, we first optimized the synthesis of two magnetic MoO₃ materials with distinct surface properties coated with PPy or PANI to be utilized in water treatment applications

86

87

88

89

90

91

92

93

94

95

96

97

98

99

100

101

102

103

104

105

106

107

using response surface methodology (RSM) to minimize the dissolution of the materials while keeping photocatalytic activity at a maximum. Subsequently, we employed small-angle neutron scattering (SANS) to monitor the growth process of PPy or PANI on these two variations of MoO₃ magnetic nanoparticles via monitoring the changes in the time-resolved radius of gyration in the polymer layer during *in situ* oxidative polymerization. The knowledge gained in this work advances the understanding on the effects of the base nanomaterial composition and chemistry in the polymer growth process, which sheds new insights into the optimization of polymer layers on the surface of the nanoparticles.

2. Experimental Section

2.1. Materials

The chemicals used in the synthesis, analysis, and photocatalytic degradation experiments were all analytical grade and were used as received. Ammonium molybdate tetrahydrate (AMT), Fe(II,III) oxide (CAS 1317-61-9), pyrrole monomer, aniline, deuterated water (D₂O), nitric acid, and ammonium persulfate were purchased from Sigma-Aldrich. Aluminum chloride used in atomic absorption spectrometry (AAS) analysis was purchased from Fisher Scientific. Methylene blue hydrate (MB, 96%) was purchased from Acros Organics. A USP grade ethanol was purchased from Recon Lab, Inc. All stocks, standards, and aqueous solutions were prepared by using Milli-O water unless otherwise noted.

2.2. Methods

2.2.1. Material Optimization and Validation

To optimize the concentration of the MoO₃, Fe₃O₄, and PPy or PANI materials to obtain a maximum percentage removal of methylene blue (MB) dye degradation and minimum dissolution

of MoO₃, a numerical optimization technique, response surface methodology, was utilized. Details on the optimization process and results using response surface methodology are presented in the Supporting Information, which include a statistical analysis of the resulting models (Table S1), contour plots of the PPy@MoO₃@Fe₃O₄ model (Figure S1), and contour plots of the PANI@MoO₃@Fe₃O₄ model (Figure S2). Validation of the predicted models was performed by comparing the predicted values of the output response provided by the Design Expert software to the observed values from the experimental results of the optimized PPy@MoO₃@Fe₃O₄ and PANI@MoO₃@Fe₃O₄ material. Validation experiments of the optimized conditions were performed in triplicates, and the materials were characterized as described below.

2.2.2. Photocatalytic Degradation Experiments for Nanoparticle Optimization and Validation

The photocatalytic degradation experiments were performed by using an initial MB concentration of 40 ppm as previously described.(4) Then, either PPy@MoO3@Fe3O4 (PMF1) or PANI@MoO3@Fe3O4 (PMF2) was added to achieve a final concentration of 500 ppm of the photocatalyst.(4,25) The MB dye solution was stirred at room temperature with an agitation speed of 180 rpm and was allowed to undergo adsorption—desorption process in a dark environment to attain equilibrium for 30 min.(4) The dark environment was achieved by covering the vials with aluminum foil to prevent passage of light into the MB dye solution. After equilibrating, the MB dye solution was irradiated by using visible light (Philips F4T5 Soft White, 4 W, intensity 199 lm) with mechanical stirring to start photodegradation. Samples of MB dye solution (0.5 mL) were withdrawn at different time intervals. Prior to analysis, the catalyst in the solution was separated by magnetic separation followed by microcentrifugation using an Eppendorf centrifuge (5415C) for 2 min at 13000 rpm. Each batch of the experiment was done in triplicate under identical conditions. 0.1 mL of the withdrawn samples was transferred in a 96-well plate and analyzed with

a UV-vis spectrometer (Biotek SynergyMX Microtiter plate reader) using a target wavelength of 664 nm. A standard curve consisting of different concentrations of MB was used to determine the relationship of the MB dye's concentration and its absorbance. Then, the percentage of dye removal was computed by using the formula

% MB dye removal =
$$\left(\frac{A_0 - A}{A_0}\right) \times 100 = \left(\frac{C_0 - C}{C_0}\right) \times 100$$
 (1)

where A_0 and C_0 are the initial absorbance and initial concentration of the sample and A and C are the absorbance and concentration of the sample at time t, respectively.

2.2.3. Dissolution Experiments for Nanoparticle Optimization and Validation

All dissolution experiments were conducted under neutral pH maintained at room temperature under static conditions. An aliquot of 500 ppm PMF1 or PMF2 photocatalyst was prepared by dispersing the photocatalyst (7.5 mg) in Milli-Q water (15 mL) in a 15 mL centrifuge tube. The solution was stored for 48 h in the dark to allow the dissolution to take place. Then, the samples were filtered through a 0.2 µm syringe-drive PES Filter Media (VWR sterile syringe filter) into an Amicon centrifugation tube (Ultra-15, Millipore), which subsequently was centrifuged at a speed of 4200 rpm for 15 min (Thermo Scientific Sorval Legend XTR centrifuge). The samples were then analyzed by using a PerkinElmer AANalyst 200 atomic absorption spectrometer using a molybdenum lamp.(4)

A MoO₃ stock solution (100 ppm) was prepared by dissolving ammonium molybdate tetrahydrate (AMT) with Milli-Q water. Standard solutions were prepared by diluting the stock solution into 1, 10, 20, 30, and 40 ppm for the calculation of the calibration curve. Because the presence of Fe in the solution can depress the molybdenum signal, 0.5% aluminum chloride was added to the samples and standard solutions prior to analysis.(26)

2.2.4. Synthesis of the Optimized MoO₃@Fe₃O₄ Nanoparticles

The magnetic MoO₃@Fe₃O₄ nanocatalyst (MF1) was prepared by the precipitation method.(27) In brief, MoO₃ precursor (AMT) (5.64 g) was dissolved in Milli-Q water (50 mL). Then, Fe₃O₄, Fe(II,III) oxide (0.158 g), was added to the solution and homogenized by ultrasonication. The Fe₃O₄ utilized in this study was in the magnetite phase and was used without further modifications for the MoO₃@Fe₃O₄ synthesis. Concentrated nitric acid was introduced dropwise to the homogeneous solution under mechanical stirring until the pH of the solution reached 1.5. The mixture was heated in a water bath at 70 °C for 8 h with mechanical stirring. After heating and stirring, the mixture was allowed to cool to room temperature. For the MoO₃@Fe₃O₄ (MF2), a modified procedure from our previous publication was utilized.(4) In this case, AMT (2.46 g) was dissolved in Milli-Q water (20 mL). Then, Fe₃O₄ (0.1 g) was dispersed in the solution, which was subsequently sonicated for 15 min to eliminate any aggregates. The mixture was introduced to an oil bath at 90 °C and put under high stirring. Once the temperature of the mixture reached 90 °C, nitric acid (5 mL) was added slowly. The material was kept at 90 °C for 3 h under high stirring to allow the MoO₃ to nucleate and grow on the surface of the magnetite. Each precipitate, MF1 and MF2, was collected by magnetic separation using a strong magnet and washed with Milli-Q water several times and then washed with 70% ethanol. The MF1 precipitate was dried in a vacuum at 60 °C (Isotemp Vacuum Oven Model 282A ThermoScientific), and the MF2 precipitate was oven-dried at 60 °C.

2.2.5. Synthesis of the Optimized Polymer-Coated Nanoparticles

The synthesis of PPy@MoO₃@Fe₃O₄ (PMF1) was done by *in situ* oxidative polymerization.(28) An amount of 2.0 g of as-synthesized MoO₃@Fe₃O₄ (MF1) (2.0 g) was dispersed in Milli-Q water (20 mL) and placed in an ice bath (0–5 °C) with stirring. Once the

177

178

179

180

181

182

183

184

185

186

187

188

189

190

191

192

193

194

195

196

197

198

solution reached a temperature between 0 and 5 °C, pyrrole monomer (0.12 mL) was added to the solution with vigorous stirring for 30 min. Ammonium persulfate (APS) dissolved in Milli-Q water (10 mL), an oxidative agent, was added dropwise to the pyrrole solution to initiate polymerization with continuous stirring. The ratio of pyrrole monomer (Py):oxidant (APS) (vol in mL:wt in g) used in the synthesis was 1:2. The polymerization process was continued overnight while maintaining the temperature at 0–5 °C. The black precipitate was collected by magnetic separation using a strong magnet and washed with 70% ethanol followed by Milli-Q water several times to remove the excess APS. The black precipitate was vacuum-dried at 60 °C.

For the synthesis of PANI@MoO3@Fe3O4, a modified procedure similar to that of the synthesis of PMF1 and PANI-CeO₂ was followed.(29) MoO₃@Fe₃O₄ (MF2) (1.012 g) was dispersed in 2 M HCl (10 mL) and then sonicated for 15 min by using the bath sonicator. In the meantime, APS (234.1 mg) was dissolved in HCl (10 mL), and aniline (100 μL) was dispersed in 10 mL of 2 M HCl. The three solutions were placed in an ice bath, and their temperatures were allowed to equilibrate to that of the ice bath over a period of 30 min. The MoO₃@Fe₃O₄ mixture was placed under high stir in the ice bath prior to the addition to the aniline solution. Lastly, the APS solution was added dropwise. The mixture was kept in the ice bath under high stir for 2 h to allow for the polymerization of aniline on the MoO₃@Fe₃O₄ material. The resulting PANI@MoO₃@Fe₃O₄ (PMF2) was cleaned by centrifugation using Milli-Q water and dried overnight at 50 °C. The high-level synthesis procedure of the PMF1 and PMF2 particles is shown in Scheme 1.

200

201

202

203

204

205

206

207

208

209

210

211

212

213

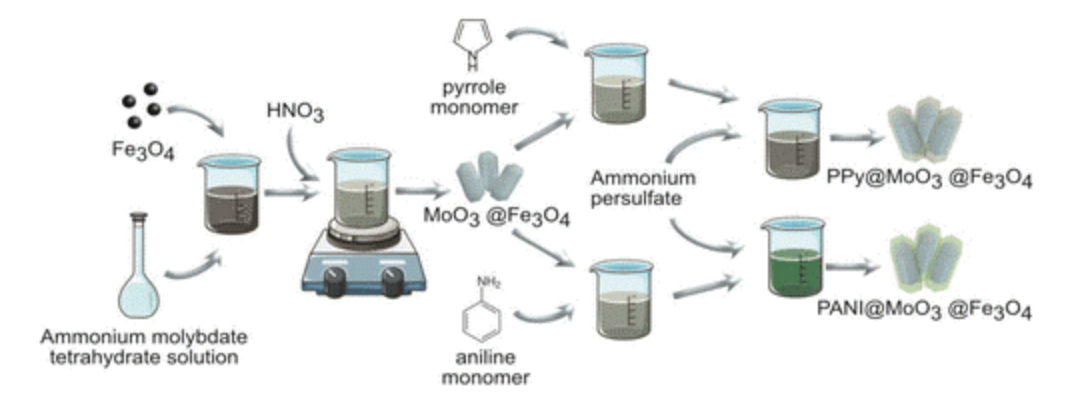
214

215

216

217

218



Scheme 1. Schematic Representation of the Synthesis Procedure of PPy@MoO3@Fe3O4 and

PANI@MoO3@Fe3O4

2.2.6. Characterization of the Nanoparticles

Morphological analysis of MoO₃@Fe₃O₄ and polymer-coated MoO₃@Fe₃O₄ was conducted by using SEM (Nova NanoSEM 230). Each sample was initially coated with gold for 30 s by using a Denton Desk V gold coater and then observed with the SEM at an accelerating voltage of 5 kV at varying magnifications. Crystallographic analysis of each material was performed by utilizing XRD (Rigaku MiniFlex 600 diffractometer with a Cu anode set to 40 kV and 15 mA and run with a scanning rate of 0.05°/s from 5° to 80° in 2θ). The XRD data were analyzed by using Match 3.0 and x'Pert Highscore Plus software to obtain crystallographic parameters such as the crystal size, lattice strain, microstrain, and dislocation density.(30,31) The surface chemical states were analyzed by using XPS (PHI Quantera SXM scanning X-ray microprobe with Al Kα (1486.6 eV) as the excitation source). The XPS measurements were calibrated by using C 1s 284.8 eV. The area ratio, spin–orbit splitting, and full width halfmaximum (FWHM) parameters were considered in the deconvolution of the spectra.(32) The functional groups present in the samples were determined by using an ATR-FTIR spectrometer (Nicolet iS10 mid-infrared FTIR spectrometer by Thermo Fisher Scientific, USA).

2.2.7. Polymer Growth Kinetics Monitored Using SANS

239

240 To monitor the growth kinetics of aniline and pyrrole in situ, SANS was utilized. These 241 experiments were conducted at the Oak Ridge National Laboratory using the General Purpose 242 SANS instrument.(33,34) Three configurations with different combinations of neutron wavelength 243 (λ) and sample-detector distance (SDD) were set to cover the scattering wavevector q range $0.001-0.4 \text{ Å}^{-1}$ for static scans. These configurations were $\lambda = 12 \text{ Å}$, SDD = 19 m, $\lambda = 4.75 \text{ Å}$, SDD 244 = 6.8 m, and λ = 4.75 Å, SDD = 1.2 m. The kinetics scans were performed with λ = 4.75 Å and 245 SDD = 6.8 m to cover the q range $0.001-0.02 \text{ Å}^{-1}$. The time binning feature of SANS data 246 247 reduction was used to obtained 5 min scans. To analyze the polymerization of aniline and pyrrole 248 on MF1 and MF2, similar procedures to the synthesis of the PMF1 and PMF2 materials utilized 249 in the RSM validation experiments and characterization were employed. However, amounts of 250 materials were altered (scaled down to 1/16th) while keeping the molar ratios the same, and 251 deuterated water was used instead of Milli-O water to accommodate the SANS instrumentation 252 and to increase the contrast. Briefly, for PMF1, MF1 (0.125 g) was dispersed in deuterated water 253 (1.25 mL) and placed in an ice bath. Then, pyrrole monomer (7.5 µL) was added to the solution. 254 Subsequently, APS solution (0.625 mL) made by dissolving 240.0 mg of APS (250.0 mg) in 255 deuterated water (10 mL) was added to the mixture. Finally, part of the mixture (1 mL) was 256 transferred to the reaction cell equipped on a tumbler for analysis. For PMF2, MF2 (63.25 mg) 257 was dispersed in 2 M HCl (0.625 mL) in deuterated water, sonicated for 15 min, and placed in an 258 ice bath. Subsequently, aniline monomer (6.25 µL) was added to 2 M HCl in deuterated water 259 (0.625 mL), and this solution was mixed into the MF2 suspension. Next, the APS solution (0.625 260 mL) made by dissolving APS (234.1 mg) in 2 M HCl with deuterated water (10 mL) was added to 261 the mixture. Finally, part of the mixture (1 mL) was transferred to the reaction cell equipped on a

tumbler for analysis. Two additional materials were analyzed with SANS, PMF3 and PMF4. PMF3 was synthesized by using the same procedure as with PMF1; however, the base material of PMF1 (MF1) was replaced with MF2. Similarly, PMF4 was synthesized via the same procedure as PMF2; however, the base material of PMF2 (MF2) was replaced with MF1. The additional samples were analyzed to allow us to investigate how the base material affects the polymerization process of each polymer. Samples were loaded on quartz reaction cells equipped on a tumbler for analysis. The SANS instrument was set to take measurements of the sample every 5 min for a maximum of 2 h at a set temperature of 2 °C. The resulting scattering data were analyzed and modeled by using the Igor64 software with the unified fitting tools from the Irena tool suite.(35–38) In the Irena unified model, each structural level of the unified equation contains two main terms, a Guinier exponential form and a structurally limited power law, where the sum of those terms allows us to approximate the intensity, *I*, at specific *Q* values (eq 2).(39,40)

$$I(Q) \cong \sum_{i=1}^{n} \left(G_i \exp \left(\frac{-Q^2 R_{g,i}^2}{3} \right) + B_i \exp \left(\frac{-Q^2 R_{g,i+1}^2}{3} \right) Q_i^{*P_i} \right) + Bkgd$$
(2)

where

$$Q^* = \frac{Q}{\left[\operatorname{erf}\left(\frac{kQR_{g,i}}{\sqrt{6}}\right) \right]^3}$$
(3)

is an error function to provide a smooth transition between the Guinier regime and the Porod regime. G_i and B_i are prefactors for the Guinier exponential and power law terms, respectively, $R_{g,i}$ is the radius of gyration of the structure feature, and P_i describes the fractal dimension of the material. Bkgd arises from the incoherent scattering background of the samples.

By optimizing each parameter, we obtained a reasonably accurate approximation of the radius of gyration of the polymer layer.

3. Results and Discussion

3.1. Validation of the Nanomaterial Synthesis

The response surface methodology (RSM) software that uses a numerical optimization technique was employed to obtain the optimum concentrations of the ammonium molybdate tetrahydrate (AMT), Fe₃O₄, and PPy or PANI when synthesizing PPy@MoO₃@Fe₃O₄ (PMF1) and PANI@MoO₃@Fe₃O₄ (PMF2), by maximizing the removal of methylene blue (MB) dye and minimizing material dissolution. To verify the validity of the models and to test the optimized materials, a set of validation experiments (MB removal and dissolution analysis) were performed. For both PMF1 and PMF2 the validation experiment results (presented in Table S2) indicated that the observed values for the MB dye degradation agree with the predicted values for both PMF1 and PMF2, respectively. PMF1 exhibited 95.39% removal of MB dye in light and 70.26% removal in dark, which agreed with the predicted values. The dissolution of 4.12%, however, was better than the predicted value. In contrast, PMF2 showed 75.98% removal of MB dye in light, 60.18% removal in dark, and 5.6% dissolution, which showed no statistical significance when compared with the predicted values. Hence, based on these results, PMF1 exhibited better removal rates of MB and higher stability than PMF2.

To gain a better understanding of the polymer coatings' benefits on the nanoparticles, comparison of the uncoated and coated materials was also performed (Figure 1). Significant reduction in dissolution occurred when MF1 and MF2 were coated with PPy and PANI, respectively. The photocatalytic activity upon addition of PPy and PANI showed similar

improvements, demonstrating improved MB removal when exposed to low power (4 W) visible light when compared to other studies (Table S3). In the case of PPy addition, photocatalytic activity increased, while MB dye adsorption showed no significant changes between the uncoated and coated material after the polymer coating (MF1 and PMF1, respectively). The increase of MB removal during photocatalysis indicates that PPy acts as a photosensitizer, which could have aided the transfer of electrons to the conduction band of MoO₃.(15) Similarly, the PANI coating on MF2 demonstrated improved photocatalytic activity, indicating PANI is also beneficial in the photocatalytic process, albeit to a lesser extent than PPy. Likely, the synergistic interaction between MoO₃ and PPy was better than that of MoO₃ and PANI. It is also possible that the black color of PPy allowed improved light absorption compared to the green color of PANI, which ultimately affected the photocatalytic activity of the material. (41) In this case, since more photons could reach the PMF1 material, more electron hole pairs could be created, consequently increasing the reactive oxygen species present in the solution, which allowed better degradation of MB. Overall, based on the results, both materials showed high MB removal in light and improved stability in water because of the introduction of the different polymer coatings, demonstrating the added benefits of the coatings to the nanoparticles.

304

305

306

307

308

309

310

311

312

313

314

315

316

317

318

319

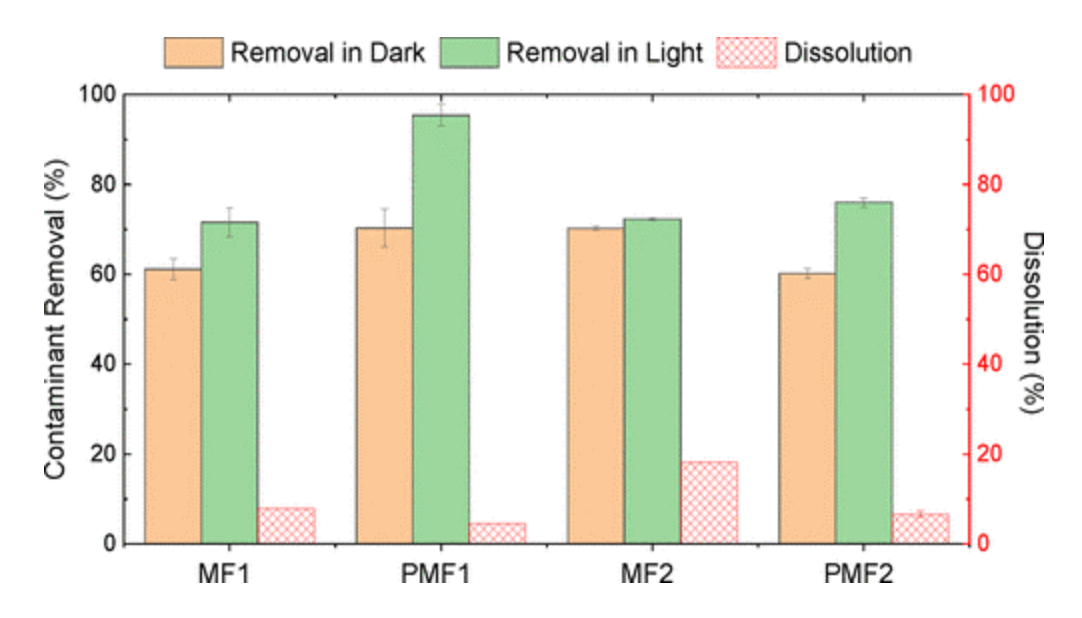


Figure 1. Methylene blue removal in light and dark and dissolution after 3 h by uncoated and coated materials (MF1, PMF1, MF2, and PMF2).

3.2. Material Surface Morphology and Chemistry

3.2.1. Optimized Material Morphology

Scanning electron microscopy (SEM) images were acquired at each step of the PMF1 and PMF2 synthesis process (Figure 2). The estimated particle size diameters of MoO₃@Fe₃O₄-1 (MF1) ranged from 0.34 to 1.34 μ m and from 0.24 to 1.25 μ m for MoO₃@Fe₃O₄-2 (MF2). Qualitatively, the magnetite appeared have low polydispersity, to while MoO₃@Fe₃O₄ materials (MF1 and MF2) presented larger polydispersity (Figure 2a). MF1 (Figure 2b) displayed an increased particle size homogeneity as opposed to MF2 (Figure 2c), which can be attributed to the increased length of time in the synthesis of the material. The increased reaction time in solution allows the material to undergo a ripening process, such as Ostwald ripening or intraparticle growth.(42) After coating the MF1 with PPy, the size distribution of the material decreased, and the apparent smoothness of the material surface became more variable (Figure 2d). Similarly to PMF1, the surface of MF2 became rougher after the polymerization process of aniline

321

322

323

324

325

326

327

328

329

330

331

332

333

334

335

336

(Figure 2e), indicating successful formation of PANI on MF2. Compared with PMF1, PMF2 showed a lower polydispersity than MF2, which was attributed to additional ripening occurring under the acidity of the solution in the PANI coating process and slower start of reaction indicated by the color of the solution.



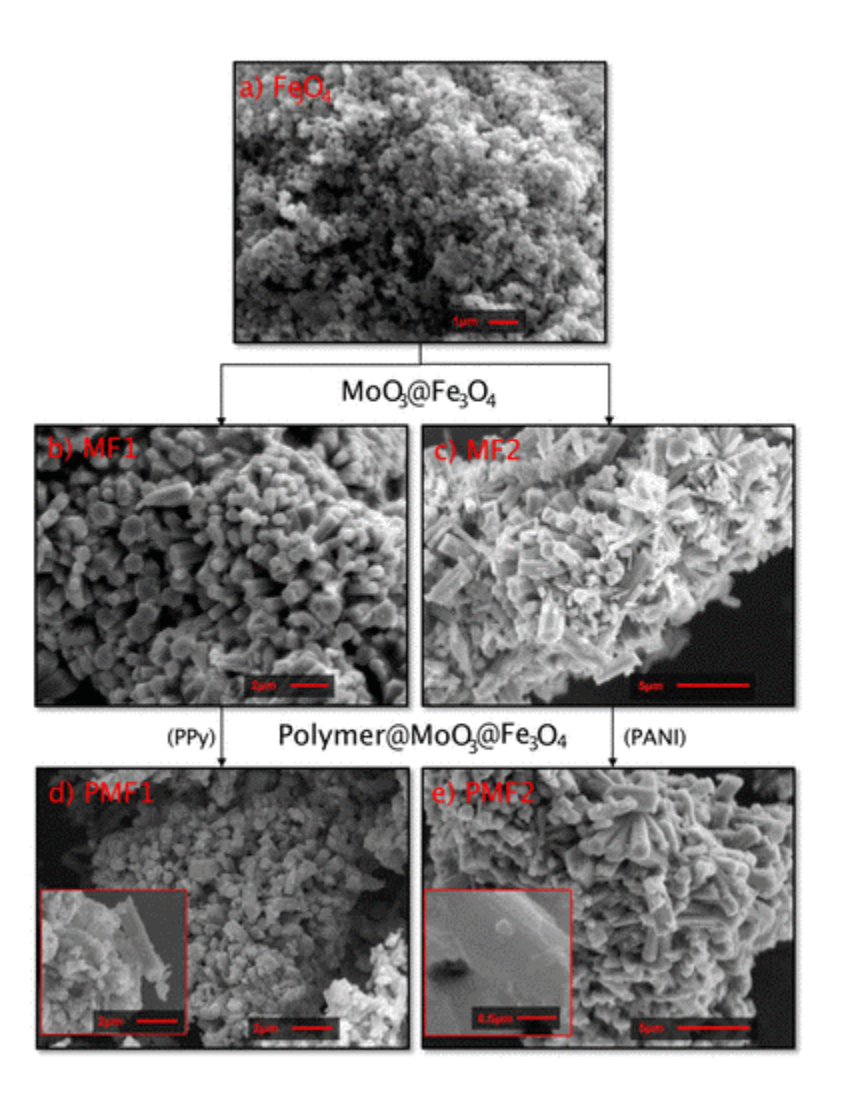


Figure 2. Scanning electron microscope images showing the morphology of (a) Fe₃O₄ (10000× magnification), (b) MF1 (6500× magnification), (c) MF2 (5000× magnification), (d) PMF1 (magnification of 7000× for the large image and 6000× showing a large PPy-coated particle), and (e) PMF2 (magnification of 5000× for the large image and 27000× for the magnified image).

3.2.2. Crystal Structures

The crystal structure and phase formation of the synthesized nanoparticles were measured by the X-ray diffraction (XRD) patterns. The XRD patterns of the Fe₃O₄, MF1, PMF1, MF2, and PMF2 shown in Figure 3 were correlated by using Match 3.0 Software.



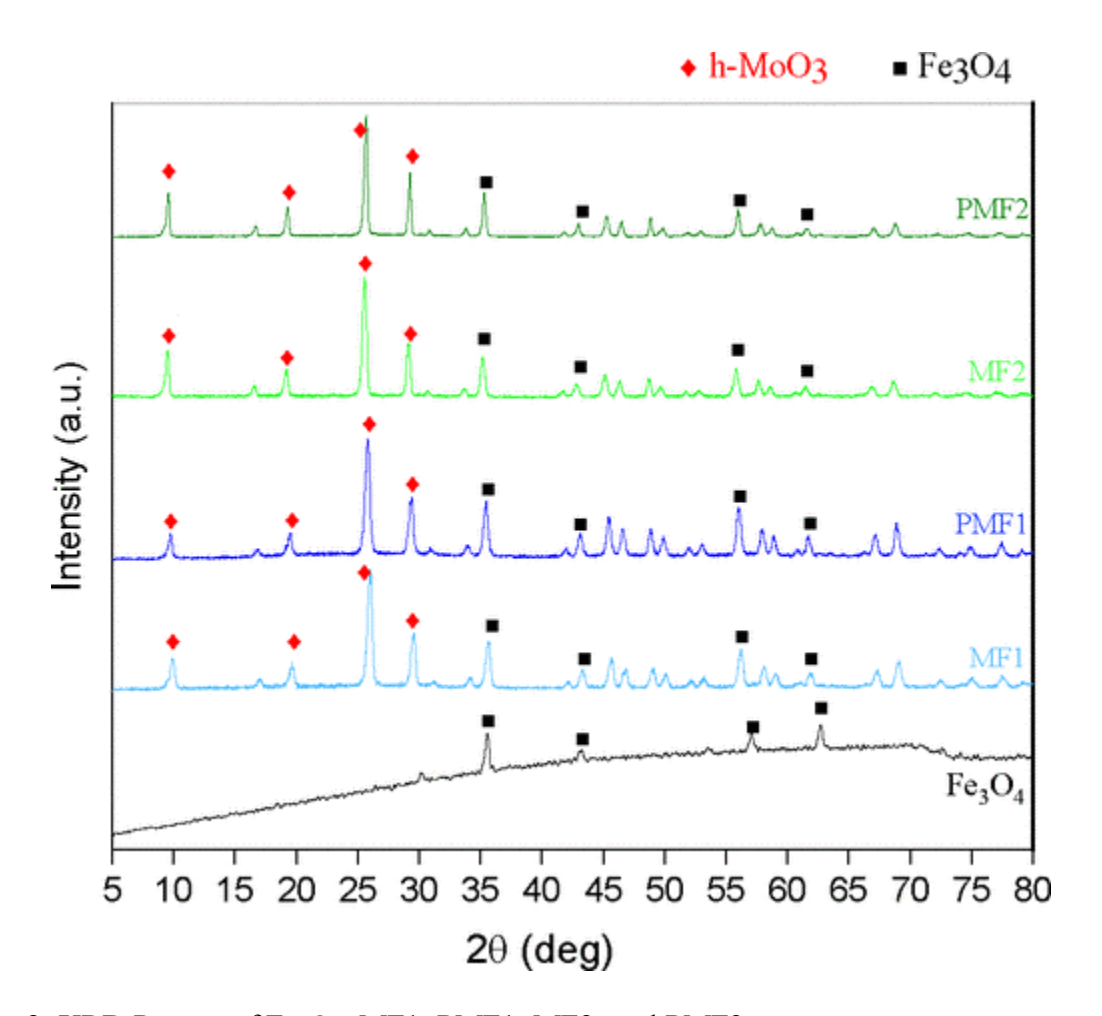


Figure 3. XRD Pattern of Fe₃O₄, MF1, PMF1, MF2, and PMF2.

The XRD pattern of Fe₃O₄ shows sharp diffraction peaks at $2\theta = 35.7^{\circ}$, 63.1° , 57.5° and 43.4° , which were assigned to the *hkl* values to planes (311), (404), (511), and (400), respectively. These diffraction peaks matched well with the 2θ calculated by the Match software, which is based

on the Crystallography Open Database (COD) entry number 96-900-6248 (COD 9006247) and indexed as the cubic crystal Fe₃O₄ system.

The hexagonal structure of MoO₃ was confirmed with the XRD spectra of MF1 and MF2, which were in good correlation with the spectra from the Crystallography Open Database (COD) entry number 96-431-6778 (COD 4316777).(43) The detectable peaks were located at $2\theta = 9.9^{\circ}$, 25.9°, 29.6°, and 19.8° for MF1 and at $2\theta = 9.6$ °, 25.7°, 29.3°, and 19.4° for MF2, indicating hkl values of (100), (210), (111), and (200). Peaks of Fe₃O₄ were also observed in the spectra. The average crystal sizes of the MF1, PMF1, MF2, and PMF2 nanomaterials were calculated using the Scherrer equation and were found to be 26, 32, 37, and 44 nm, respectively.(30,31) Additional crystallographic parameters are presented in Table S4. The XRD patterns for both PMF1 and PMF2 showed that the peaks for MoO₃ in MF1 and MF2 were maintained, respectively, even after the addition of polypyrrole (PMF1) and polyaniline (PMF2). In addition, the peak position hardly changed, which indicates that polymerization of polypyrrole and polyaniline took place on the surface of MF1 and MF2.(17) The sharp and detectable peaks indicate that the synthesized nanostructures were well-crystallized. Diffraction peaks of Fe₃O₄ had a lower intensity compared to the diffraction peaks of MoO₃ due to the small amount of Fe₃O₄ present in the MF and PMF nanostructures. In Figure S3, there was a slight distortion and broadening of peaks in PMF1 between 20° and 30°, indicating the presence of amorphous PPy.(15,19) The PANI peaks in Figure 3 and Figure S4 decreased in intensity due to the polymerization of PANI on the surface of MF1.(44) Furthermore, a slight broad curvature of baseline at ~25° was observed, which was ascribed to the amorphous nature of PANI; however, this change is subtle due to the highly crystalline nature of the metal oxide. (44) There was no further observation of diffraction peaks in the spectra, which indicated that the PPy and PANI do

360

361

362

363

364

365

366

367

368

369

370

371

372

373

374

375

376

377

378

379

380

381

not hinder the crystalline behavior of MF. The presence of the polymers PPy and PANI in PPy@MoO₃@Fe₃O₄ and PANI@MoO₃@Fe₃O₄ was further confirmed through ATR-FTIR analysis.

3.2.3. Surface Components

383

384

385

386

387

388

389

390

391

392

393

394

395

396

397

398

399

400

401

402

403

404

405

X-ray photoelectron spectroscopy (XPS) was utilized to determine the chemical state of the key surface components, such as molybdenum and carbon. The survey spectra of the magnetite, the uncoated magnetic MoO₃ materials, and the polymer-coated materials are shown in Figure 4. The Fe peaks were clearly present in the Fe₃O₄ spectra but were not as apparent in the coated materials.(45) This was expected given that the magnetite is in the core of the material and XPS detailed analysis performance of embedded components (>10 nm) is limited as it is a surfacesensitive technique.(46) In the MoO₃@Fe₃O₄ materials (MF1 and MF2) the Mo 3d_{3/2} and Mo 3d_{5/2} peaks were clearly present. Carbon and nitrogen peaks were also observed. Nitrogen was likely introduced during the synthesis process since nitric acid was utilized to allow the nucleation and growth of MoO₃. In the PMF2 spectra, a peak at Cl 2p was detected, indicating introduction of Cl⁻ ions in the material. The carbon peak can be attributed to adventitious carbon as well as small amounts of carbon impurities in the material. In the polymer-coated materials (PMF1 and PMF2), the carbon peaks became more prominent, as expected, due to the high carbon content of the polymers. In particular, the relative carbon content for MF1, MF2, PMF1, and PMF2 was calculated to approximately 13.6%, 19.1%, 31.3%, and 51.2%, respectively (additional relative atomic concentrations are shown in Table S5). This large increase of the relative carbon content in PMF1 and PMF2 as compared to MF1 and MF2 was indicative of the successful coating of PPy on MF1 and PANI on MF2.

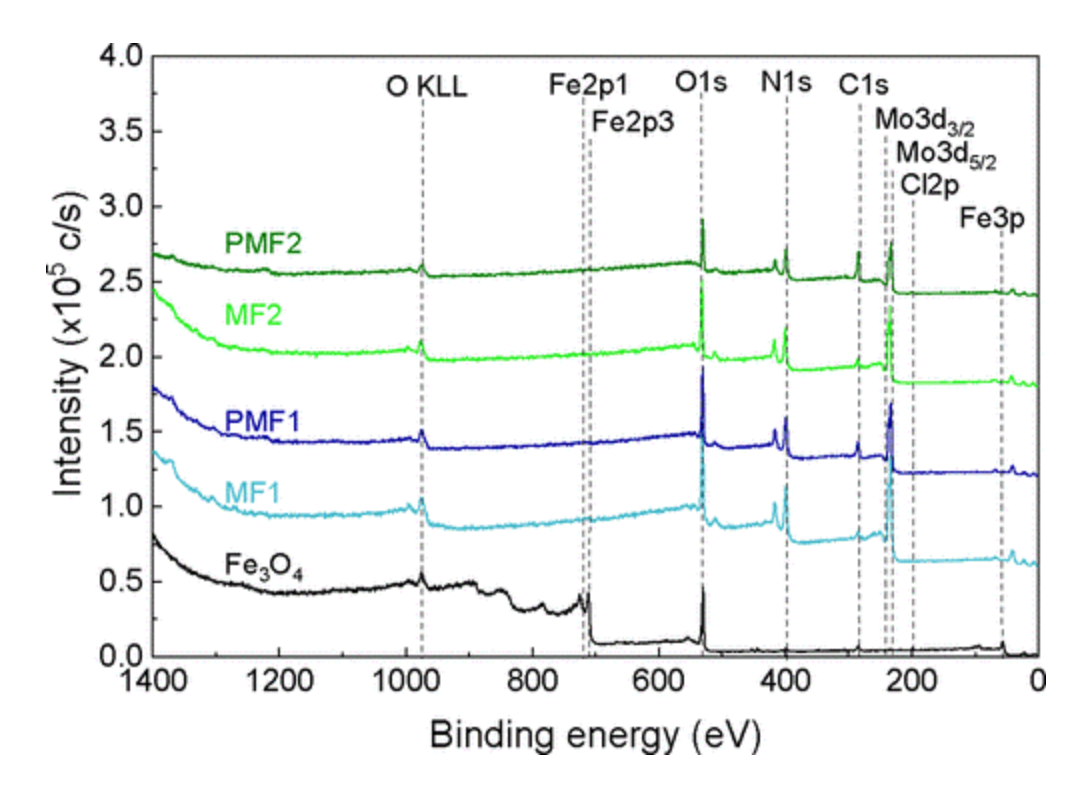


Figure 4. XPS spectra of Fe₃O₄, MF1, PMF1, MF2, and PMF2, each offset by 60×10^3 c/s.

To further analyze the surface components of the uncoated MoO₃@Fe₃O₄ and the polymer-coated MoO₃@Fe₃O₄, detailed spectra of the carbon and molybdenum spectra were acquired. Fe 2p spectra were also acquired and successfully verified the incorporation of Fe₃O₄ (Figure S5). The Mo 3d spectra of the uncoated MoO₃@Fe₃O₄ are shown in Figure 5. MoO₃ is the primary photocatalytic component of the material, and its oxidation state has been shown to directly affect the photocatalytic properties of the material.(4) A high Mo⁶⁺ to Mo⁵⁺ ratio indicates increased photocatalytic activity.(4) The beneficial effect of oxygen vacancies, resulting from the introduction of Mo⁵⁺ states, toward the photocatalytic activity of the material is owed to the narrowing of the bandgap due to delocalized states in the valence band overlapping with the valence band. The reduced bandgap increases light absorption in the visible spectral region, thus enhancing the material's photocatalytic activity.(4) While the increased amount of oxygen

vacancies is beneficial in lowering the bandgap of the material, which can increase photocatalysis via increasing light absorption, it can also increase absorption of light by midgap states reducing the generation of excitons.(4) The reduction of excitons lessens the number of reactive oxygen species generated by the material, thus reducing its photocatalytic activity.

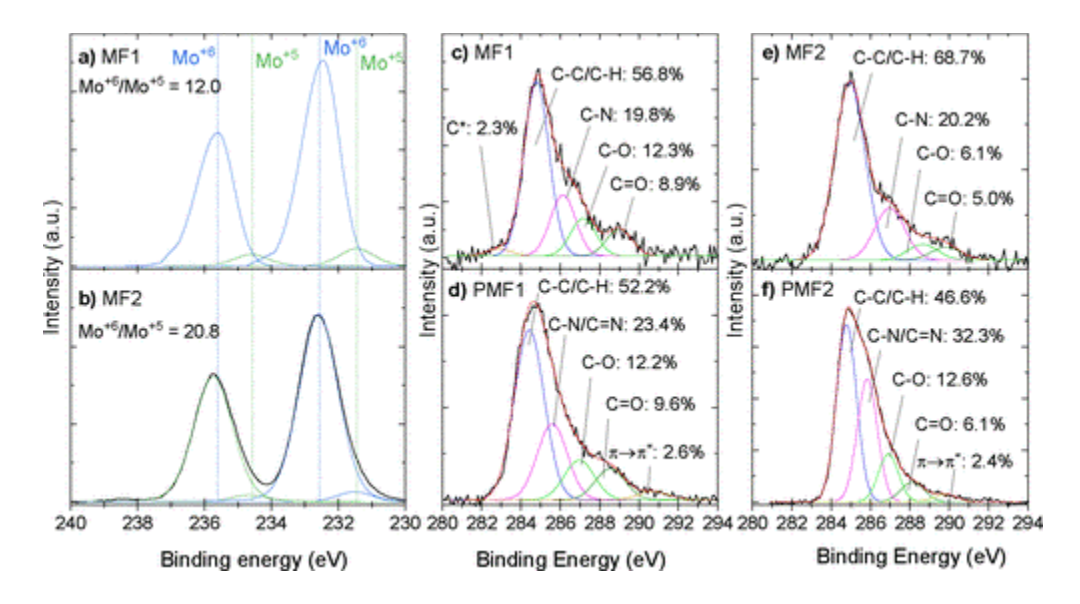


Figure 5. XPS Mo 3d spectrum and fittings of (a) MF1 and (b) MF2. XPS C 1s spectra of (c) MF1, (d) PMF1, (e) MF2, and (f) PMF2.

The fitted Mo 3d spectra of MF1 and MF2 and the percentage of each component present are shown in Figure 5 with additional information presented in Table S6. For MF1 and MF2 the ratio of Mo⁶⁺ to Mo⁵⁺ was 12.0 and 20.8, respectively. Interestingly, the Mo⁶⁺ to Mo⁵⁺ ratio for MF2 was similar to that of the nanorods synthesized by using a similar procedure,(4) indicating that the addition of the magnetic core had minimal influence on the chemical structure of MoO₃. Rather, the amounts of the starting material, temperature, and reaction duration were the main factors contributing to the chemical differences. Furthermore, the magnetite particles, which are positively charged under acidic pH, can act as nucleation centers for MoO₃ formation assisting in

the reaction process and altering the growth of the particles. While MF1 had a lower ratio of Mo⁶⁺ to Mo⁵⁺ than MF2, the photocatalytic activity of PMF1 was greater than that of PMF2, as shown in Table S2. This could be due to the fact that PPy, a black polymer, could favor light absorption more than PANI, a dark green polymer.(41)

The changes of the carbon bond types in the polymerization are shown in Figure 5 (the core-level oxygen spectra, which also show the incorporation of C, are depicted in Figure S6). The peaks at ~284.8 eV in MF1 and MF2 correspond to carbon impurities or adventitious carbon.(32,47) In PMF1 and PMF2, however, this peak is indicative of the presence of benzenoid rings from the polymers coated on the nanoparticles.(48) Furthermore, the peaks at approximately 285.8, 287, and 288.5 eV were assigned to C-N/C=N/=C-NH⁺, C-O, and C=O bonds, respectively, which were present in PMF1 and PMF2.(49,50) The peaks at 290.7 and 290 eV for PMF1 and PMF2, respectively, were attributed to the π - π * transition component (shake-up signal) in the PPy or PANI aromatic rings.(50)

3.2.4. Material Components

The ATR-FTIR analysis was conducted to further show the successful coating of polymers on the nanoparticles. The FTIR spectra of the Fe₃O₄, MF1, PMF1, MF2, and PMF2 in the range of 2000–450 cm⁻¹ are shown in Figure 6 and the spectra information for each of the materials is presented in Table S7. The bands between 600 and 450 cm⁻¹ in the Fe₃O₄ and MoO₃ spectra in Figure 6 resulted from the metal–oxygen vibrations. In particular, the characteristic band for Fe₃O₄ at 559.9 cm⁻¹ corresponding to the torsion and vibration mode of the Fe–O bonds,(51) and bands at 517.3 and 568.4 cm⁻¹ in the MoO₃ spectra corresponding to the Mo–O–Mo bending vibrations were observed.(4,28) In addition, bands corresponding to the M=O stretching vibrations were present in the MoO₃ spectra at 878.9 and 895.3 cm⁻¹.(52,53) The band at 1403.5

cm⁻¹ in the MoO₃ spectra indicates N–H bending of NH₄⁺ groups in the structure.(52) In the PPy spectra, the bands at 1042.8 and 1305.1 cm⁻¹ were assigned to C–H stretching vibrations, and the bands at 1174.5 and 1461.8 cm⁻¹ and the PPy characteristic band at 1552.4 cm⁻¹ were assigned to C–N stretching vibrations and aromatic ring vibrations, respectively.(54) In the case of the PANI spectra, characteristic bands indicative of the emeraldine oxidation of PANI were observed. In particular, the C=N stretching band of the quinoid diamine unit at 1564.7 cm⁻¹ and the C–C aromatic ring stretching band of the benzenoid diamine unit at 1488.3 cm⁻¹ were present.(55) Furthermore, peaks at 1296 and 1245 cm⁻¹ were present due to the C–N stretching of secondary aromatic amine bonds (56) and C–N⁺ stretching vibrations,(57,58) respectively. In addition, the 797.5 cm⁻¹ peak was designated to the out-of-plane C–H bond deformation on the 1,4-disubstituted rings in PANI.(56)

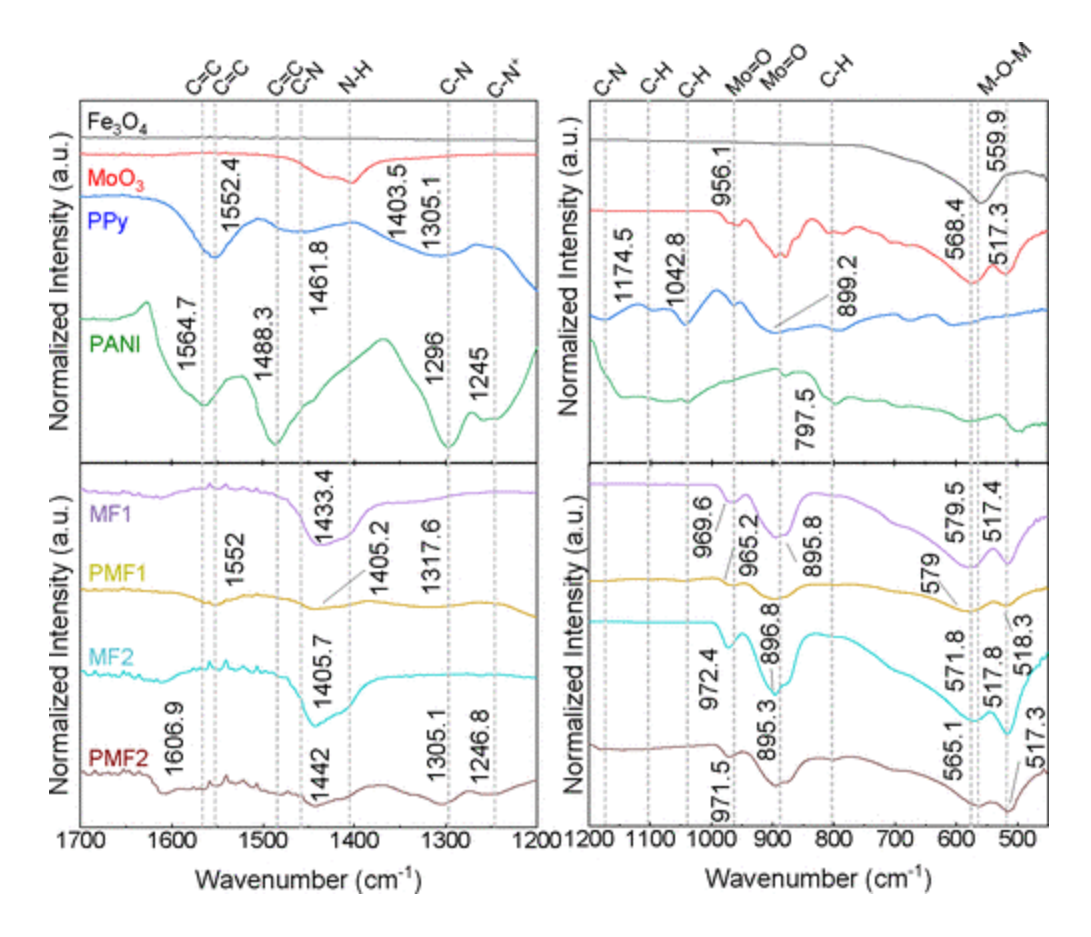


Figure 6. ATR-FTIR spectra of Fe₃O₄, MoO₃, MF1, PMF1, MF2, and PMF2 from top to bottom. Presence of carbon–carbon (C–C), carbon–hydrogen (C–H), carbon–nitrogen (C–N, C=N, C–N, C–N⁺), nitrogen–hydrogen (N–H), molybdenum–oxygen (Mo–O), and metal–oxygen–metal (M–O–M such as Mo–O–Mo and iron–oxygen–iron) bonds are indicated in the spectra.

When Fe₃O₄ was incorporated into MoO₃, the M–O–M (metal–oxygen–metal single bonds) and Mo=O bands were preserved. Additionally, there was a broadening and intensity increase in the N–H bending peak of MoO₃ at 1403.5 cm⁻¹ from the inclusion of ammonium ions (NH₄⁺).(52,59) When MF1 was coated with PPy, there was a dampening of the M=O and M–O–M peaks as well as peaks corresponding to C=C stretching vibrations and C–H in-plane vibrations, which are indicative of the coating of PPy on MF1.(28) Likewise, in the case of MF2 being coated

with PANI, there was also a decrease in the intensity of the Mo=O and M-O-M peaks. In addition, peaks corresponding to C-N stretching of the secondary aromatic amine and C-N⁺ stretching appeared in the PMF2 spectra, and the peak due to the benzenoid diamine unit disappeared due to the coating of PANI on MoO₃. In the MF and PMF spectra several shifts and band changes were noticed as the MF material was coated with PPy or PANI. The N-H vibration peak in PMF1 and PMF2 vanished, while it was previously prominent in MF1 and MF2, indicating the change of NH₄⁺ present in the structure of MoO₃ to NH₃.(60) Furthermore, the Mo-O-Mo bending peaks in PMF1 and PMF2 underwent slight blue-shifts, the C-N stretching vibration of PPy showed a clear blue-shift in PMF1 and PMF2, and the C-N stretching peak underwent a red-shift, indicating strong intermolecular interactions by N-Mo in PMF1 and PMF2, likely as a result of hydrogen bonding or van der Waals attraction forces.(61)

3.2.5. Polymerization Kinetics on the Surface of the Nanoparticles

The polymer chains coated on the nanoparticles not only significantly altered the stability of these materials in water but also affected their absorptive and photocatalytic capabilities. Monitoring the kinetics of polymer growth on such materials can help us understand the effects of the base materials' composition and chemistry on the polymer growth process, which is critical for tuning parameters to optimize the properties of the materials in their broad applications.

In this study, we used *in situ* SANS to monitor the growth of polymers on the surface of the nanoparticles. SANS data were collected when either pyrrole or aniline polymerized on MF1 and MF2 to examine how the polymerization of PPy and PANI is affected by the base nanomaterial. The SANS profile and model fitting of each sample at the end of the polymerization are shown in Figure 7 and Table S8, respectively. The materials exhibited a multilevel structure, which is

reflected by the multiple "knees" and linear regions on the log-log plots of the SANS curves. The curves were fitted by using the unified exponential model.(35,40,62)



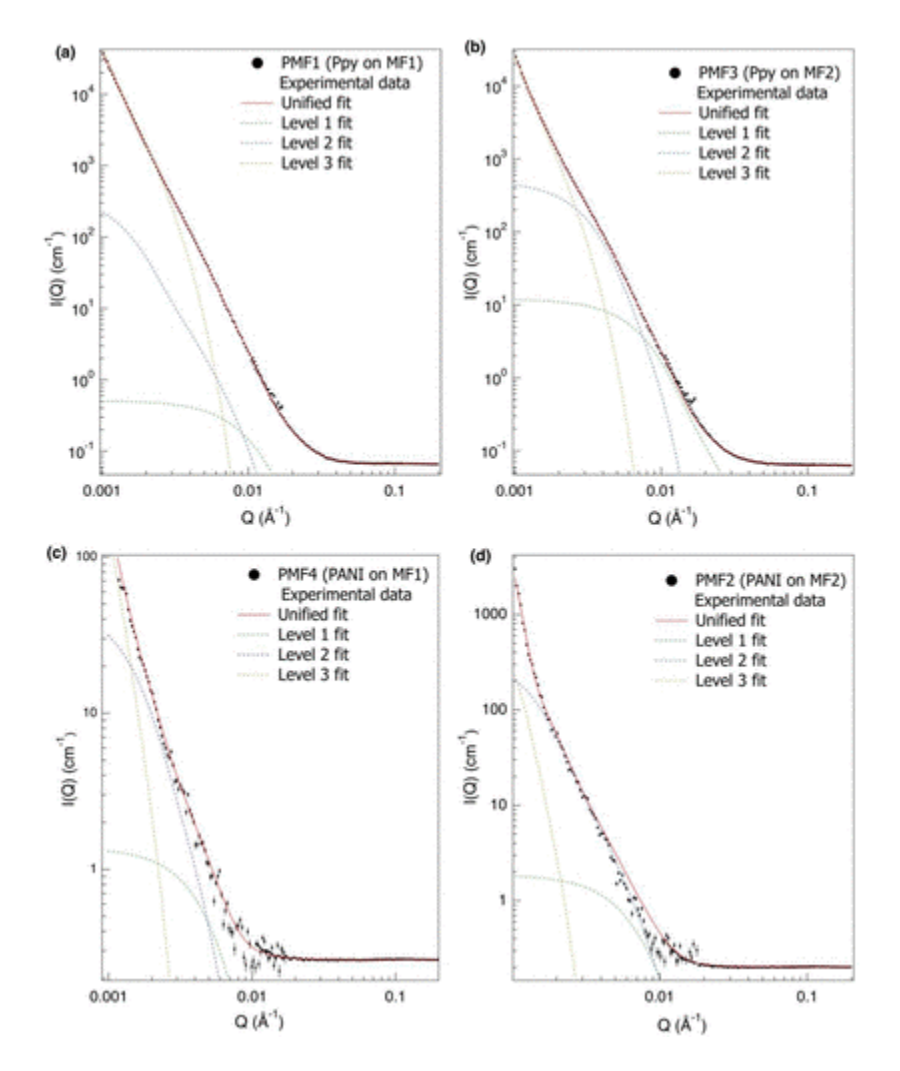


Figure 7. SANS profiles after polymerization are completed for (a) PMF1 (PPy on MF1), (b) PMF3 (PPy on MF2), (c) PMF4 (PANI on MF1), and (d) PMF2 (PANI on MF2). The solid red line corresponds to the model fitting using eq 2. The decomposed contribution from each level is displayed as dotted lines.

Each scattering curve was modeled by using three structural levels as shown in Figure 7. However, PMF2 (PANI on MF2) had a fourth structural level. The fourth structural level located in the low-Q region in PMF2 (Figure 7d) indicated the presence of larger structures in the PMF2 data compared to other samples (PMF1, PMP3, and PMF4). Such structures may arise from large nanoparticle aggregates; unfortunately, the size of these aggregates cannot be determined by SANS since it is outside the instrument's resolution.(39) The structural features corresponding to levels 1 and 3 arose from the base material (MF1 or MF2) as P exponent values between 3 and 4 indicate a surface fractal type for these levels. (62) The $R_{\rm g}$ of the level 3 fell between 274 and 300 nm. The level 2 structure was ascribed to the polymer chains on the material considering the P exponents fell between 1.5 and 3, corresponding to the mass fractals of polymer chains.(62) This region changed the most during the polymerization process as evidenced by the $R_{\rm g}$ changes. In Table S8, the final R_g values of level 2 after the polymerization ended were 56.1 ± 0.56 , 136.9 ± 0.92 , 63.5 \pm 0.22, and 124.5 \pm 3.6 nm for PMF1 (PPy on MF1), PMF2 (PANI on MF2), PMF3 (PPy on MF2), and PMF4 (PANI on MF1), respectively. The different R_g values indicate that polymer type and base material's surface properties influenced the polymer chain growth, agreeing with previous reports in which R_g was found to depend on the base material surface, polymer type, and the original concentration of the base material in the solution. (63) The growth of the PPy and PANI chains on the surface of the base materials as a function of

The growth of the PPy and PANI chains on the surface of the base materials as a function of time is shown in Figure 8. PPy polymerization initiated faster yet had a slower rate than PANI, while PPy was more affected by the base material properties than PANI polymerization. These observations resulted from the differences in polymerization mechanisms between the two polymers. In the mechanism of PPy growth, oxidation of pyrrole monomers led to the formation of positively charged dimers. (64) The negative charge of MoO₃ offered a strong electrostatic

515

516

517

518

519

520

521

522

523

524

525

526

527

528

529

530

531

532

533

534

535

536

attraction toward the pyrrole dimers promoting polymerization as the dimers could readily attach to the negatively charged surface of MoO₃, which initiated the polymer chain growth (Figure 9a). The polymerization rate was hindered, however, by the competitive interaction between the dimers attaching to MoO₃ and attaching to each other to form longer chains. PANI's chain growth was much faster than that of PPy once polymerization started. Polymerization of aniline on both base materials started after 60 min, which was consistent with our visual observation of solution color change. PANI formation mechanism is affected by many factors (acidity, monomer concentration, temperature, etc.) and is still controversial.(65) To initiate polymerization, aniline needs to be oxidized to cation radicals. These radicals have different resonating forms with varying reactivities, which may result in the formation of diverse chain architectures. (65) Furthermore, the acidity of the media impacts the degree of protonation of oligomers, which may lead to a different reaction pathway, thereby altering polymerization kinetics. (65) Our results were consistent with the theory behind aniline polymerization in acidic media in which oligomer nucleates form slowly.(21,66) This induction period can be very slow depending on the starting temperature and acidity of the media; however, the subsequent polymerization rate is rapid.(20,21,66) In highly acidic solutions, intermediate compounds are thought to be formed in the induction period (iminoquinonid compounds consisting of compounds similar to nigraniline pernigraniline).(67) The intermediates act as strong oxidants due to their protonation in acidic media. (67) However, rather than oxidizing aniline, which is a neutral compound, such protonated compounds can preferentially react with the MF surface in areas in which oxygen vacancies generate donor states and, as a consequence, prolong the induction period. The reactivities of the species that participate in the PPy polymerization process and the PANI polymerization process are vastly different, which led to the changes in polymerization initiation and rate depicted

538

539

540

541

542

543

544

545

546

547

548

549

550

551

552

553

554

555

556

557

558

559

in Figure 9. Additionally, the polymerization process not only depends on the rate of the reactions but it also depends on adsorption equilibrium constants.(20) Competitive interaction between oligomers and nucleates adsorbing on the surface of the MF material and assembling with other oligomers or nucleates can further slow polymer chain growth initiation and affect polymerization rate.

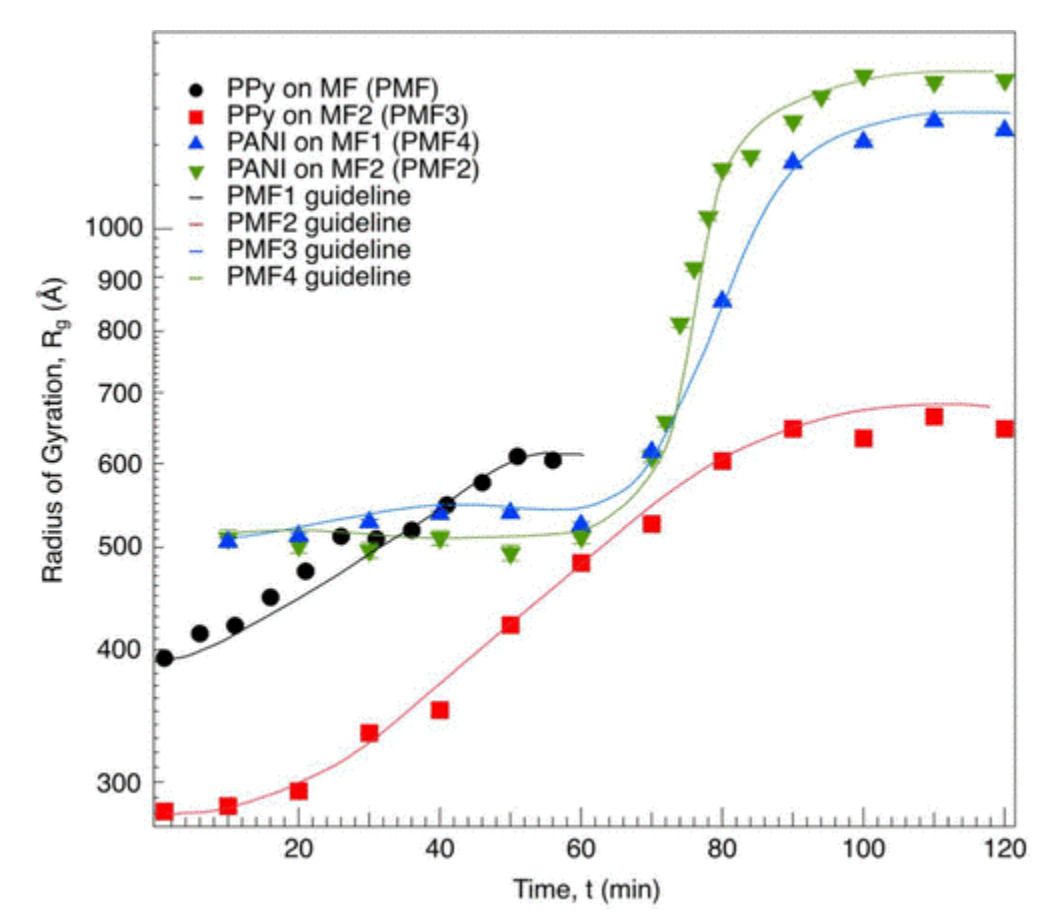


Figure 8. Radius of gyration as a function of time from the fitted curves of each polymer-coated

material.

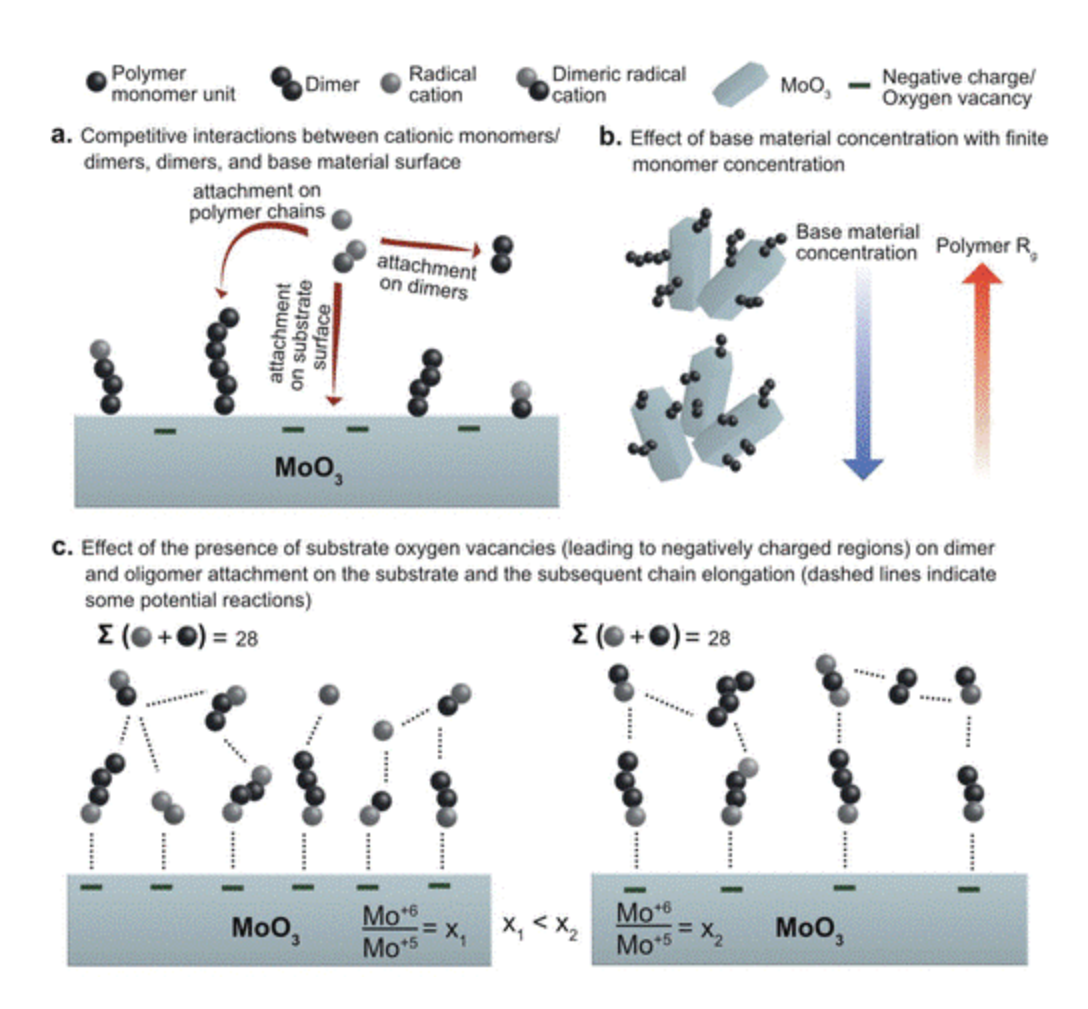


Figure 9. Base material effects on polymer formation: (a) attachment of cationic species on the base material competes with their attachment on existing polymer chains or oligomers, (b) increased base material concentration can lead to larger polymers, and (c) a decrease in oxygen vacancies leads to longer chains on average due to the reduction of potential attachment points on the base material surface.

The ultimate size of polymer chains grafted on nanoparticles largely depended on the concentration of the nanoparticles. The size of PANI chains after the polymerization ended was almost double the PPy chain size. In the PPy polymerization process, the concentration of the base material was much larger than the base material concentration in PANI chain growth (0.66 and

0.34 g/mL, respectively). Because of the greater amount of available substrate surface present and the fixed monomer concentration in PPy polymerization, the average polymer chain length was expected to be shorter (Figure 9b), which was consistent with the SANS results. The difference in monomer structure between pyrrole and aniline is another factor that can affect the final chain length of the grafted polymers. PPy exhibits a zigzag shape while PANI has a straight conformation (Scheme S1). If the polymerization number is the same, the final size of PANI is expected to be longer than that of PPy.

An important similarity between the polymerization of PPy and PANI on MF1 and MF2 was the tendency of the material that had MF1 as the core to result in a smaller final R_g of polymers. Because the difference in size of MF1 and MF2 was subtle, the determining factor in the magnitude of R_g could be associated with the surface chemistry of the base material. Material defects in the MoO₃ structure, in particular oxygen vacancies, are capable of enhancing dimer attachment as well as promoting pyrrole and aniline monomer oxidation due to their higher surface reactivity, which facilitates the generation of donor or acceptor states.(1,68) As shown in the XPS analysis of the MoO₃ in MF1 and MF2, MF1 presented a larger number of oxygen vacancies than MF2 as indicated by the smaller Mo⁶⁺:Mo⁵⁺ ratio. Thus, the MF1 surface was more reactive than the MF2 surface, which could have promoted monomer oxidation or provided attachment centers for PPy dimers or PANI oligomers (Figure 9c). Therefore, an increase in PPy and PANI R_g and rate of polymerization on MF2 rather than on MF1 was expected, which was consistent with the SANS results.

Furthermore, polymerization for both PPy and PANI could be enhanced or hindered depending on the reaction conditions (monomer, oxidant, substrate material concentrations, media acidity, etc.). Because of their polycationic nature, their oligomers preferentially adsorb on

hydrophobic areas of surfaces.(66) Hydrophobicity in a material is introduced by oxygen vacancies(69) supporting our data that showed increased surface adsorption of either PANI or PPy on MF1 rather than MF2 due to the higher amount of oxygen vacancies present in the MF1 structure (Figure 9c). Additionally, the $R_{\rm g}$ growth can be affected by the uniformity via which the oligomers attached on each surface. Chain attachment tends toward higher uniformity when the surface is more hydrophobic, which leads to the formation of polymer brush-type structures rather than granular ones.(66) While the charge differences between MF1 and MF2 was unlikely to change the architecture formed, a more ordered attachment allowed more oligomers to adsorb on the surface of the material. Thus, for MF1, the higher number of oligomers attaching to its surface resulted in the formation of shorter chains due to the fixed availability of monomers in solution and increased probability of polymer growth termination. (70) Furthermore, the increase in density of polymer chains on the surface of MF1 hindered the polymerization rate likely due to the increase mass-transfer-limited of reactions at the surface rather than reaction-limited polymerization. (70) As such, polymer length and polymerization rate were reduced, and the final R_g was smaller for MF1 rather than MF2.

4. Conclusion

605

606

607

608

609

610

611

612

613

614

615

616

617

618

619

620

621

622

623

624

625

626

627

In this study, we developed two visible-light photocatalytic magnetic MoO₃ nanomaterials, with varying oxygen vacancies, which were coated with conducting polymers (PPy or PANI) to decrease the solubility of the nanomaterials and increase their photocatalytic properties, improving their utility in water treatment. Furthermore, we monitored the polymerization kinetics of the nanomaterials to elucidate how the surface chemistry of base materials, in particular oxygen vacancies, would affect polymerization of pyrrole and aniline. Our results revealed that particle surface chemistry can have numerous effects, including the promotion of monomer oxidation,

enhancement of dimer or oligomer adsorption on the surface of the particle, and oligomer attachment uniformity. Despite the complexity of polymer growth on nanostructured materials, neutron scattering allowed us to form a more concrete theory on the polymerization kinetics of two conjugated polymers.

632

633

628

629

630

631

Abbreviations

- 634 PPy polypyrrole
- 635 PANI polyaniline
- 636 MF MoO₃@Fe₃O₄
- PMF1 PPy@MoO3@Fe3O4
- PMF2 PANI@MoO3@Fe3O4
- 639 VOC volatile organic compound
- 640 RSM response surface methodology
- 641 SANS small-angle neutron scattering
- 642 AMT ammonium molybdate tetrahydrate
- 643 AAS atomic absorption spectrometry
- 644 MB methylene blue
- 645 APS ammonium persulfate
- 646 Py pyrrole monomer
- 647 SEM scanning electron microscopy
- 648 XPS X-ray photoelectron spectroscopy
- 649 COD crystallography open database
- $R_{\rm g}$ radius of gyration

651

652

653

654

655

Supporting Information

Response surface methodology material design and results, XRD and XPS analysis supplementary figures and tables, ATR-FTIR peaks table, SANS fitting curve values table, and polypyrrole and polyaniline and related monomers chemical structures scheme

656

657

658

659

660

661

662

663

664

665

666

667

668

669

670

671

672

673

Acknowledgments

This work was partially supported by NSF BEINM Grant 170551, the Welch Foundation Grant E-2011-20190330, U.S. Department of Energy, Office of Science, Office of Workforce Development for Teachers and Scientists, Office of Science Graduate Student Research (SCGSR) program and the Engineering Research and Development for Technology (ERDT) Sandwich Program of the College of Engineering, University of the Philippines, Diliman. The SCGSR program is administered by the Oak Ridge Institute for Science and Education (ORISE) for the DOE. ORISE is managed by ORAU under Contract DE-SC0014664. This research used resources at the High Flux Isotope Reactor, a DOE Office of Science User Facility operated by the Oak Ridge National Laboratory. All opinions expressed in this paper are the author's and do not necessarily reflect the policies and views of DOE, ORAU, or ORISE. The findings achieved herein are solely the responsibility of the authors. We thank Dr. Ali Ansari for providing the XRD and ATR-FTIR measurements as well as Drs. Janire Peña-Bahamonde and Hoang Nguyen for the SEM images. This manuscript has been authored by UT-Battelle, LLC, under Contract DE-AC05-00OR22725 with the U.S. Department of Energy. The United States Government retains and the publisher, by accepting the article for publication, acknowledges that the United States Government retains a nonexclusive, paid-up, irrevocable, worldwide license to publish or

- 674 reproduce the published form of this manuscript, or allow others to do so, for United States
- 675 Government purposes. The Department of Energy will provide public access to these results of
- 676 federally sponsored research in accordance with the DOE Public Access Plan
- 677 (http://energy.gov/downloads/doe-public-access-plan).

678

679

References

- de Castro, I. A.; Datta, R. S.; Ou, J. Z.; Castellanos-Gomez, A.; Sriram, S.; Daeneke, T.;
- Kalantar-zadeh, K. Molybdenum Oxides From Fundamentals to Functionality. Adv.
- Mater. 2017, 29, 1701619, DOI: 10.1002/adma.201701619
- Zheng, L.; Xu, Y.; Jin, D.; Xie, Y. Novel Metastable Hexagonal MoO3 Nanobelts:
- 684 Synthesis, Photochromic, and Electrochromic Properties. Chem. Mater. 2009, 21 (23),
- 685 5681–5690, DOI: 10.1021/cm9023887
- Fanourakis, S. K.; Peña-Bahamonde, J.; Bandara, P. C.; Rodrigues, D. F. Nano-Based
- Adsorbent and Photocatalyst Use for Pharmaceutical Contaminant Removal during Indirect
- Potable Water Reuse. npj Clean Water 2020, 3 (1), 1, DOI: 10.1038/s41545-019-0048-8
- Peña-Bahamonde, J.; Wu, C.; Fanourakis, S. K.; Louie, S. M.; Bao, J.; Rodrigues, D. F.
- Oxidation State of Mo Affects Dissolution and Visible-Light Photocatalytic Activity of
- 691 MoO3 Nanostructures. J. Catal. 2020, 381, 508–519, DOI: 10.1016/j.jcat.2019.11.035
- Liu, H.; Qu, J.; Zhang, T.; Ren, M.; Zhang, Z.; Cheng, F.; He, D.; Zhang, Y. nan. Insights
- into Degradation Pathways and Toxicity Changes during Electro-Catalytic Degradation of
- Tetracycline Hydrochloride. Environ. Pollut. 2020, 258, 113702, DOI:
- 695 10.1016/j.envpol.2019.113702
- 696 6 Shahab-ud-Din; Ahmad, M. Z.; Qureshi, K.; Bhatti, I. A.; Zahid, M.; Nisar, J.; Iqbal, M.;

- 697 Abbas, M. Hydrothermal Synthesis of Molybdenum Trioxide, Characterization and
- Photocatalytic Activity. Mater. Res. Bull. 2018, 100, 120–130, DOI:
- 699 10.1016/j.materresbull.2017.11.044
- 700 7 El-Salamony, R. A.; Gobara, H. M.; Younis, S. A. Potential Application of MoO3 Loaded
- 701 SBA-15 Photo-Catalyst for Removal of Multiple Organic Pollutants from Water
- 702 Environment. J. Water Process Eng. 2017, 18, 102–112, DOI: 10.1016/j.jwpe.2017.06.010
- 703 8 Zhang, Y.; Park, S. J. Bimetallic AuPd Alloy Nanoparticles Deposited on MoO3 Nanowires
- for Enhanced Visible-Light Driven Trichloroethylene Degradation. J. Catal. 2018, 361,
- 705 238–247, DOI: 10.1016/j.jcat.2018.03.010
- Adhikari, S.; Lee, H. H.; Kim, D. H. Efficient Visible-Light Induced Electron-Transfer in
- z-Scheme MoO3/Ag/C3N4 for Excellent Photocatalytic Removal of Antibiotics of Both
- 708 Ofloxacin and Tetracycline. Chem. Eng. J. 2020, 391, 123504, DOI:
- 709 10.1016/j.cej.2019.123504
- 710 10 Jing, X.; Peng, X.; Sun, X.; Zhou, W.; Wang, W.; Wang, S. Design and Synthesis of
- 711 Mo2C/MoO3 with Enhanced Visible-Light Photocatalytic Performance for Reduction of Cr
- 712 (VI) and Degradation of Organic Pollutants. Mater. Sci. Semicond. Process. 2019, 100,
- 713 262–269, DOI: 10.1016/j.mssp.2019.05.004
- 714 11 Balakumar, V.; Kim, H. H.; Manivannan, R.; Kim, H. H.; Ryu, J. W.; Heo, G.; Son, Y. A.
- 715 Ultrasound-Assisted Method to Improve the Structure of CeO2@polyprrole Core-Shell
- Nanosphere and Its Photocatalytic Reduction of Hazardous Cr6+. Ultrason. Sonochem.
- 717 2019, 59, 104738, DOI: 10.1016/j.ultsonch.2019.104738
- 718 12 Liu, Y.; Zhang, B.; Yang, Y.; Chang, Z.; Wen, Z.; Wu, Y. Polypyrrole-Coated α-
- MoO3Nanobelts with Good Electrochemical Performance as Anode Materials for Aqueous

- 720 Supercapacitors. J. Mater. Chem. A 2013, 1 (43), 13582–13587, DOI: 10.1039/c3ta12902k
- Ling, Y.; Cao, T.; Liu, L.; Xu, J.; Zheng, J.; Li, J.; Zhang, M. Fabrication of Noble Metal
- Nanoparticles Decorated on One Dimensional Hierarchical Polypyrrole@MoS2
- 723 Microtubes. J. Mater. Chem. B 2020, 8 (34), 7801–7811, DOI: 10.1039/D0TB01387K
- 724 14 Ates, M. A Review Study of (Bio)Sensor Systems Based on Conducting Polymers. Mater.
- 725 Sci. Eng., C 2013, 33 (4), 1853–1859, DOI: 10.1016/j.msec.2013.01.035
- 726 15 Zia, J.; Kashyap, J.; Riaz, U. Facile Synthesis of Polypyrrole Encapsulated
- V2O5Nanohybrids for Visible Light Driven Green Sonophotocatalytic Degradation of
- 728 Antibiotics. J. Mol. Liq. 2018, 272, 834–850, DOI: 10.1016/j.molliq.2018.10.091
- 729 16 Yadav, A.; Kumar, H.; Sharma, R.; Kumari, R. Influence of Polyaniline on the
- Photocatalytic Properties of Metal Nanocomposites: A Review. Colloids Interface Sci.
- 731 Commun. 2021, 100339, DOI: 10.1016/j.colcom.2020.100339
- 732 17 Dhanavel, S.; Nivethaa, E.; Narayanan, V.; Stephen, A. Visible Light Induced
- Photocatalytic Degradation of Methylene Blue Using Polyaniline Modified Molybdenum
- 734 Trioxide. Mechanika 2017, 9 (April), 1–6
- 735 18 Sundaram, M. M.; Sangareswari, M.; Muthirulan, P. Enhanced Photocatalytic Activity of
- Polypyrrole/TiO2 Nanocomposites for Acid Violet Dye Degradation under UV Irradiation.
- 737 Int. J. Innov. Res. Sci. Eng. 2014, 2347–3207
- 738 19 Xu, J.; Hu, Y.; Zeng, C.; Zhang, Y.; Huang, H. Polypyrrole Decorated BiOI Nanosheets:
- 739 Efficient Photocatalytic Activity for Treating Diverse Contaminants and the Critical Role
- of Bifunctional Polypyrrole. J. Colloid Interface Sci. 2017, 505, 719–727, DOI:
- 741 10.1016/j.jcis.2017.06.054
- Mezhuev, Y. O.; Korshak, Y. V.; Shtil'man, M. I. Effect of Poly(Ethylene Oxide) on the

- Kinetics of Oxidative Polymerization of Aniline. Russ. J. Gen. Chem. 2016, 86 (11), 2520–
- 744 2525, DOI: 10.1134/S1070363216110190
- 745 21 Sapurina, I.; Stejskal, J. The Mechanism of the Oxidative Polymerization of Aniline and the
- Formation of Supramolecular Polyaniline Structures. Polym. Int. 2008, 57 (12), 1295–
- 747 1325, DOI: 10.1002/pi.2476
- 748 22 Wu, C.; Zhou, S. Light Scattering Study of Spherical Poly(N-Isopropylacrylamide)
- 749 Microgels. J. Macromol. Sci., Part B: Phys. 1997, 36 (3), 345–355, DOI:
- 750 10.1080/00222349708212388
- 751 23 Scherrenberg, R.; Coussens, B.; van Vliet, P.; Edouard, G.; Brackman, J.; de Brabander, E.;
- Mortensen, K. The Molecular Characteristics of Poly(Propyleneimine) Dendrimers as
- 753 Studied with Small-Angle Neutron Scattering, Viscosimetry, and Molecular Dynamics.
- 754 Macromolecules 1998, 31 (2), 456–461, DOI: 10.1021/ma9618181
- 755 24 Liu, Y.; Feng, P.; Wang, Z.; Jiao, X.; Akhtar, F. Novel Fabrication and Enhanced
- Photocatalytic MB Degradation of Hierarchical Porous Monoliths of MoO3 Nanoplates.
- 757 Sci. Rep. 2017, 7 (1), 1845, DOI: 10.1038/s41598-017-02025-3
- 758 25 Silvestri, S.; Ferreira, C. D.; Oliveira, V.; Varejão, J. M. T. B.; Labrincha, J. A.; Tobaldi,
- D. M. Synthesis of PPy-ZnO Composite Used as Photocatalyst for the Degradation of
- Diclofenac under Simulated Solar Irradiation. J. Photochem. Photobiol., A 2019, 375, 261–
- 761 269, DOI: 10.1016/j.jphotochem.2019.02.034
- Levinson, A. A. Analytical Methods for Atomic Absorption Spectrophotometry. Geochim.
- 763 Cosmochim. Acta 1969, 33 (10), 1315–1316, DOI: 10.1016/0016-7037(69)90053-2
- 764 27 Zhou, Q.; Fu, S.; Zou, M.; He, Y.; Wu, Y.; Wu, T. Deep Oxidative Desulfurization of Model
- 765 Oil Catalyzed by Magnetic MoO3/Fe3O4. RSC Adv. 2015, 5 (85), 69388–69393, DOI:

- 766 10.1039/C5RA11028A
- 767 28 Zhang, X.; Zeng, X.; Yang, M.; Qi, Y. Investigation of a Branchlike MoO3/Polypyrrole
- Hybrid with Enhanced Electrochemical Performance Used as an Electrode in
- Supercapacitors. ACS Appl. Mater. Interfaces 2014, 6 (2), 1125–1130, DOI:
- 770 10.1021/am404724u
- 771 29 Liu, C.; Tai, H.; Zhang, P.; Yuan, Z.; Du, X.; Xie, G.; Jiang, Y. A High-Performance
- Flexible Gas Sensor Based on Self-Assembled PANI-CeO2 Nanocomposite Thin Film for
- 773 Trace-Level NH3 Detection at Room Temperature. Sens. Actuators, B 2018, 261, 587–597,
- 774 DOI: 10.1016/j.snb.2017.12.022
- 775 30 Chander, S.; Dhaka, M. S. Impact of Thermal Annealing on Physical Properties of Vacuum
- Evaporated Polycrystalline CdTe Thin Films for Solar Cell Applications. Phys. E 2016, 80,
- 777 62–68, DOI: 10.1016/j.physe.2016.01.012
- 778 31 Sundeep, D.; Gopala Krishna, A.; Ravikumar, R. V. S. S. N.; Vijaya Kumar, T.; Daniel
- Ephraim, S.; Pavan, Y. L. Spectral Characterization of Mechanically Synthesized MoO3-
- 780 CuO Nanocomposite. Int. Nano Lett. 2016, 6 (2), 119–128, DOI: 10.1007/s40089-015-
- 781 0178-z
- 782 32 Pérez-González, M.; Tomás, S. A. Surface Chemistry of TiO2-ZnO Thin Films Doped with
- Ag. Its Role on the Photocatalytic Degradation of Methylene Blue. Catal. Today 2021, 360,
- 784 129–137, DOI: 10.1016/j.cattod.2019.08.009
- Wignall, G. D.; Littrell, K. C.; Heller, W. T.; Melnichenko, Y. B.; Bailey, K. M.; Lynn, G.
- 786 W.; Myles, D. A.; Urban, V. S.; Buchanan, M. V.; Selby, D. L.; Butler, P. D. The 40 m
- 787 General Purpose Small-Angle Neutron Scattering Instrument at Oak Ridge National
- 788 Laboratory. J. Appl. Crystallogr. 2012, 45 (5), 990– 998, DOI:

- 789 10.1107/S0021889812027057
- 790 34 Heller, W. T.; Cuneo, M.; Debeer-Schmitt, L.; Do, C.; He, L.; Heroux, L.; Littrell, K.;
- Pingali, S. V.; Qian, S.; Stanley, C.; Urban, V. S.; Wu, B.; Bras, W. The Suite of Small-
- Angle Neutron Scattering Instruments at Oak Ridge National Laboratory. J. Appl.
- 793 Crystallogr. 2018, 51 (2), 242–248, DOI: 10.1107/S1600576718001231
- 794 35 Ilavsky, J.; Jemian, P. R. Irena: Tool Suite for Modeling and Analysis of Small-Angle
- 795 Scattering. J. Appl. Crystallogr. 2009, 42 (2), 347–353, DOI:
- 796 10.1107/S0021889809002222
- 797 36 Zhang, F.; Ilavsky, J.; Long, G. G.; Quintana, J. P. G.; Allen, A. J.; Jemian, P. R. Glassy
- Carbon as an Absolute Intensity Calibration Standard for Small-Angle Scattering. Metall.
- 799 Mater. Trans. A 2010, 41 (5), 1151–1158, DOI: 10.1007/s11661-009-9950-x
- 800 37 Nelson, A. Co-Refinement of Multiple-Contrast Neutron/X-Ray Reflectivity Data Using
- 801 MOTOFIT. J. Appl. Crystallogr. 2006, 39 (2), 273–276, DOI:
- 802 10.1107/S0021889806005073
- 803 38 Beaucage, G. Approximations Leading to a Unified Exponential/Power-Law Approach to
- Small-Angle Scattering. J. Appl. Crystallogr. 1995, 28 (6), 717–728, DOI:
- 805 10.1107/S0021889895005292
- Hackley, V. A.; Stoimenov, P. K.; Ho, D. L.; Sung, L. P.; Klabunde, K. J. Structure
- Development in Aerogel-Processed Nano-Crystalline Alkaline Earth Oxides as Revealed
- by SANS. J. Appl. Crystallogr. 2005, 38 (4), 619–631, DOI: 10.1107/S0021889805015244
- 809 40 Beaucage, G.; Ulibarri, T. A.; Black, E. P.; Schaefer, D. W. ACS Symp. Ser. 1995, 585,
- 810 97–111, DOI: 10.1021/bk-1995-0585.ch009
- 811 41 Xue, T.; Tang, L.; Tang, R.; Li, Y.; Nie, J.; Zhu, X. Color Evolution of a Pyrrole-Based

- 812 Enone Dye in Radical Photopolymerization Formulations. Dyes Pigm. 2021, 188, 109212,
- 813 DOI: 10.1016/j.dyepig.2021.109212
- Thanh, N. T. K.; Maclean, N.; Mahiddine, S. Mechanisms of Nucleation and Growth of
- Nanoparticles in Solution. Chem. Rev. 2014, 114 (15), 7610–7630, DOI:
- 816 10.1021/cr400544s
- Lunk, H. J.; Hartl, H.; Hartl, M. A.; Fait, M. J. G.; Shenderovich, I. G.; Feist, M.; Frisk, T.
- A.; Daemen, L. L.; Mauder, D.; Eckelt, R.; Gurinov, A. A. Hexagonal Molybdenum
- Trioxide" Known for 100 Years and Still a Fount of New Discoveries. Inorg. Chem. 2010,
- 49 (20), 9400–9408, DOI: 10.1021/ic101103g
- 821 44 Senthilkumar, B.; Vijaya Sankar, K.; Sanjeeviraja, C.; Kalai Selvan, R. Synthesis and
- Physico-Chemical Property Evaluation of PANI-NiFe2O4 Nanocomposite as Electrodes for
- 823 Supercapacitors. J. Alloys Compd. 2013, 553, 350– 357, DOI:
- 824 10.1016/j.jallcom.2012.11.122
- 825 45 Fujii, T.; de Groot, F. M.F.; Sawatzky, G. A.; Voogt, F. C.; Hibma, T.; Okada, K. In Situ
- Xps Analysis of Various Iron Oxide Films Grown by (Formula Presented)-Assisted
- Molecular-Beam Epitaxy. Phys. Rev. B: Condens. Matter Mater. Phys. 1999, 59 (4), 3195–
- 828 3202, DOI: 10.1103/PhysRevB.59.3195
- 829 46 Tayefeh, A.; Poursalehi, R.; Wiesner, M.; Mousavi, S. A. XPS Study of Size Effects of
- Fe3O4 Nanoparticles on Crosslinking Degree of Magnetic TFN Membrane. Polym. Test.
- 831 2019, 73, 232–241, DOI: 10.1016/j.polymertesting.2018.11.037
- Huang, Y.; Cong, L.; Yu, J.; Eloy, P.; Ruiz, P. The Surface Evolution of a Catalyst Jointly
- Influenced by Thermal Spreading and Solid-State Reaction: A Case Study with an Fe2O3-
- 834 MoO3 System. J. Mol. Catal. A: Chem. 2009, 302 (1–2), 48–53, DOI:

- 835 10.1016/j.molcata.2008.11.033
- Patil, S. H.; Gaikwad, A. P.; Sathaye, S. D.; Patil, K. R. To Form Layer by Layer Composite
- Film in View of Its Application as Supercapacitor Electrode by Exploiting the Techniques
- of Thin Films Formation Just around the Corner. Electrochim. Acta 2018, 265 (March),
- 839 556–568, DOI: 10.1016/j.electacta.2018.01.165
- 840 49 Reddy, B. J.; Vickraman, P.; Justin, A. S. Microwave Synthesis of MoO3 -Reduced
- Graphene Oxide Nanocomposite for High Performance Asymmetric Supercapacitors. J.
- Mater. Sci.: Mater. Electron. 2019, 30 (4), 3618–3628, DOI: 10.1007/s10854-018-00641-
- 843 x
- Parnell, C. M.; Chhetri, B. P.; Mitchell, T. B.; Watanabe, F.; Kannarpady, G.; RanguMagar,
- A. B.; Zhou, H.; Alghazali, K. M.; Biris, A. S.; Ghosh, A. Simultaneous Electrochemical
- Deposition of Cobalt Complex and Poly(Pyrrole) Thin Films for Supercapacitor Electrodes.
- 847 Sci. Rep. 2019, 9 (1), 1–13, DOI: 10.1038/s41598-019-41969-6
- 848 51 Yusoff, A. H. M.; Salimi, M. N.; Jamlos, M. F. Synthesis and Characterization of
- Biocompatible Fe3O4 Nanoparticles at Different PH. AIP Conf. Proc. 2016, 1835, 1–5,
- 850 DOI: 10.1063/1.4981832
- 851 52 Wongkrua, P.; Thongtem, T.; Thongtem, S. Synthesis of h- and α- MoO3 by Refluxing and
- 852 Calcination Combination: Phase and Morphology Transformation, Photocatalysis, and
- Photosensitization. J. Nanomater. 2013, 2013, 1, DOI: 10.1155/2013/702679
- 854 53 Fanourakis, S. K.; Peña-Bahamonde, J.; Rodrigues, D. F. Inorganic Salts and Organic
- Matter Effects on Nanorod, Nanowire, and Nanoplate MoO3 aggregation, Dissolution, and
- 856 Photocatalysis. Environ. Sci.: Nano 2020, 7 (12), 3794–3804, DOI: 10.1039/D0EN00708K
- 857 54 Cetiner, S.; Karakas, H.; Ciobanu, R.; Olariu, M.; Kaya, N. U.; Unsal, C.; Kalaoglu, F.;

- Sarac, A. S. Polymerization of Pyrrole Derivatives on Polyacrylonitrile Matrix, FTIR-ATR
- and Dielectric Spectroscopic Characterization of Composite Thin Films. Synth. Met. 2010,
- 860 160 (11–12), 1189–1196, DOI: 10.1016/j.synthmet.2010.03.007
- 861 55 Ajeel, K. I.; Kareem, Q. S. Synthesis and Characteristics of Polyaniline (PANI) Filled by
- Graphene (PANI/GR) Nano-Films. J. Phys.: Conf. Ser. 2019, 1234 (1), 012020, DOI:
- 863 10.1088/1742-6596/1234/1/012020
- Lissarrague, M. H.; Lamanna, M. E.; D'Accorso, N. B.; Goyanes, S. Effects of Different
- Nucleating Particles on Aniline Polymerization. Synth. Met. 2012, 162 (11–12), 1052–
- 866 1058, DOI: 10.1016/j.synthmet.2011.12.018
- 867 57 Razalli, R. L.; Abdi, M. M.; Tahir, P. M.; Moradbak, A.; Sulaiman, Y.; Heng, L. Y.
- Polyaniline-Modified Nanocellulose Prepared from Semantan Bamboo by Chemical
- Polymerization: Preparation and Characterization. RSC Adv. 2017, 7 (41), 25191–25198,
- 870 DOI: 10.1039/C7RA03379F
- Shao, W.; Jamal, R.; Xu, F.; Ubul, A.; Abdiryim, T. The Effect of a Small Amount of Water
- on the Structure and Electrochemical Properties of Solid-State Synthesized Polyaniline.
- Materials 2012, 5 (10), 1811–1825, DOI: 10.3390/ma5101811
- 874 59 Chithambararaj, A.; Sanjini, N. S.; Velmathi, S.; Chandra Bose, A. Preparation of H-MoO3
- and α-MoO3 Nanocrystals: Comparative Study on Photocatalytic Degradation of
- Methylene Blue under Visible Light Irradiation. Phys. Chem. Chem. Phys. 2013, 15 (35),
- 877 14761–14769, DOI: 10.1039/c3cp51796a
- 878 60 Sen, S. K.; Paul, T. C.; Manir, M. S.; Dutta, S.; Hossain, M. N.; Podder, J. Effect of Fe-
- Doping and Post Annealing Temperature on the Structural and Optical Properties of MoO3
- Nanosheets. J. Mater. Sci.: Mater. Electron. 2019, 30 (15), 14355–14367, DOI

- 881 10.1007/s10854-019-01805-z
- Das, A. K.; Karan, S. K.; Khatua, B. B. High Energy Density Ternary Composite Electrode
- Material Based on Polyaniline (PANI), Molybdenum Trioxide (MoO3) and Graphene
- Nanoplatelets (GNP) Prepared by Sono-Chemical Method and Their Synergistic
- Contributions in Superior Supercapacitive Performance. Electrochim. Acta 2015, 180, 1–
- 886 15, DOI: 10.1016/j.electacta.2015.08.029
- 887 62 Beaucage, G. Small-Angle Scattering from Polymeric Mass Fractals of Arbitrary Mass-
- 888 Fractal Dimension. J. Appl. Crystallogr. 1996, 29 (2), 134–146, DOI:
- 889 10.1107/S0021889895011605
- 890 63 Jo, W.-K.; Kumar, S.; Isaacs, M. A.; Lee, A. F.; Karthikeyan, S. Cobalt Promoted TiO2/GO
- for the Photocatalytic Degradation of Oxytetracycline and Congo Red. Appl. Catal., B 2017,
- 892 201, 159–168, DOI: 10.1016/j.apcatb.2016.08.022
- 893 64 Tan, Y.; Ghandi, K. Kinetics and Mechanism of Pyrrole Chemical Polymerization. Synth.
- 894 Met. 2013, 175, 183–191, DOI: 10.1016/j.synthmet.2013.05.014
- 895 65 Saeb, M. R.; Zarrintaj, P.; Khandelwal, P.; Chauhan, N. P. S. Synthetic Route of Polyaniline
- 896 (I): Conventional Oxidative Polymerization; Elsevier Inc.: 2019.
- 897 66 Stejskal, J.; Sapurina, I.; Trchová, M. Polyaniline Nanostructures and the Role of Aniline
- 898 Oligomers in Their Formation. Prog. Polym. Sci. 2010, 35 (12), 1420–1481, DOI:
- 899 10.1016/j.progpolymsci.2010.07.006
- 900 67 Ciric-Marjanovic, G. Recent Advances in Polyaniline Research: Polymerization
- Mechanisms, Structural Aspects, Properties and Applications. Synth. Met. 2013, 177 (3),
- 902 1–47, DOI: 10.1016/j.synthmet.2013.06.004
- 903 68 Pacchioni, G. Oxygen Vacancy: The Invisible Agent on Oxide Surfaces. ChemPhysChem

2003, 4 (10), 1041–1047, DOI: 10.1002/cphc.200300835 904 905 69 Qi, G.; Liu, X.; Li, C.; Wang, C.; Yuan, Z. The Origin of Superhydrophobicity for 906 Intrinsically Hydrophilic Metal Oxides: A Preferential O2 Adsorption Dominated by 907 Oxygen Vacancies. Angew. Chem., Int. Ed. 2019, 58 (48), 17406- 17411, 908 10.1002/anie.201909121 909 Kang, C.; Crockett, R.; Spencer, N. D. The Influence of Surface Grafting on the Growth 70 910 Rate of Polymer Chains. Polym. Chem. 2016, 7 (2), 302-309, DOI: 10.1039/C5PY01521A